

Relaxation in an Extended Bosonic Josephson Junction

J.-F. Mennemann,^{1,2} I. E. Mazets,^{2,3} M. Pigneur,³ H. P. Stimming,¹ N. J. Mauser,¹ J. Schmiedmayer,³ and S. Erne^{3,*}

¹Research Platform MMM “Mathematics–Magnetism–Materials”, c/o Fak. für Mathematik, Univ. Wien, 1090 Vienna, Austria

²Wolfgang Pauli Institute c/o Fak. für Mathematik, Univ. Wien, Oskar-Morgenstern-Platz 1, 1090 Vienna, Austria

³Vienna Center for Quantum Science and Technology, Atominstytut, TU Wien, Stadionallee 2, 1020 Vienna, Austria

(Dated: October 16, 2021)

We present a detailed analysis of the relaxation dynamics in an extended bosonic Josephson junction. We show that stochastic classical field simulations in three spatial dimensions reproduce the main experimental findings of M. Pigneur *et al.*, Phys. Rev. Lett. **120**, 173601 (2018). We give an analytic solution describing the short time evolution through multimode dephasing. For longer times, the observed relaxation to a phase locked state is caused by nonlinear dynamics beyond the sine-Gordon model, persisting even at zero temperature. Finally, we analyze different experimentally relevant trapping geometries and their potential for analogue simulation of the sine-Gordon model out of equilibrium. Our results provide the basis for future experimental implementations aiming to study quantum effects of extended bosonic Josephson junctions.

Introduction.—Quantum field theory (QFT) is a central tool for understanding quantum many-body systems. An important way to get insight into their most fundamental properties is through exactly solvable QFT models. A prominent example is the sine-Gordon (SG) model [1, 2] which exhibits topological excitations and can be tuned from weakly interacting to strongly correlated. It appears in diverse physics settings ranging from high-energy to solid-state physics [3] such as, e.g., the Coulomb gas [4, 5] and XY-model [6], the extended Bose-Hubbard model [7], or entanglement entropy in expanding quantum fields [8]. It has been proposed in Ref. [9] that the quantum SG model can be simulated with two tunnel coupled one-dimensional (1D) bosonic superfluids (extended 1D bosonic Josephson junction), which was confirmed experimentally in thermal equilibrium [10, 11]. Understanding the non-equilibrium dynamics of the SG model, in particular in its strongly correlated regime, is a far more challenging task, experimentally as well as theoretically.

A recent experiment [12], studying an extended bosonic Josephson junction [13–15] in two 1D ⁸⁷Rb superfluids out of equilibrium, makes the situation even less trivial. The observed Josephson oscillations (of the interwell atom-number difference or of its conjugate variable, the global phase difference) were damped after only a few periods. More intriguing, this relaxation led to a phase locked state with almost straight interference fringes along the longitudinal axis of the trap. This implies local damping of oscillations within each experimental realization and relaxation beyond simple dephasing dynamics. To date, this behavior could not be explained by various microscopic models [16–18] or the SG model not only in the semiclassical, but also in the quantum [19–22] treatment.

In this letter we present a detailed numerical study of the quasicondensate dynamics, which explain the main results of the experiment [12]. For the experimentally relevant harmonic confinement we show that the system re-

laxes in two stages. The short time dynamics is fully described by multimode dephasing, already leading to a local damping of the oscillations. At longer times, we show that nonlinear dynamics beyond the SG model causes the relaxation of the system to the observed phase locked state. We find this effect to persist even at zero temperature, which highlights the importance of understanding the relevance of classical nonlinear dynamics when analyzing complex quantum many-body systems. Finally, we discuss different experimentally realizable trapping geometries to mitigate these effects.

Comparison to experiment.— In order to determine the contribution of nonlinear dynamics of classical fields, we numerically solve the Gross–Pitaevskii equation (GPE)

$$i\hbar \frac{\partial}{\partial t} \Psi(\mathbf{r}, t) = \left[-\frac{\hbar^2}{2m} \nabla^2 + V(\mathbf{r}, t) + \frac{4\pi\hbar^2 a_s}{m} |\Psi(\mathbf{r}, t)|^2 \right] \Psi(\mathbf{r}, t) \quad (1)$$

for the order parameter $\Psi(\mathbf{r}, t)$ of a quasicondensate [23]. Here m and a_s are the atom mass and s -wave scattering length of ⁸⁷Rb, respectively, and $V(\mathbf{r}, t)$ is a double-well potential with tunable barrier height and weak harmonic confinement along the (longitudinal) z -direction [24].

Within each well the motion of atoms is effectively constrained to one dimension. Tunneling through the barrier couples the two wells, realizing the extended bosonic Josephson junction in the relative phase ϕ and conjugate atom number difference $\delta\rho$ of the two condensates. For the simplest approximation the local Josephson frequency is given by $\omega_J(z) = \sqrt{4J\mu(z)/\hbar}$, with tunneling coupling J and local chemical potential $\mu(z)$ [24]. Corrections to ω_J are in general not negligible and sensitive to, e.g., the particle number N and explicit shape of $U(\mathbf{r}, t)$. Our three-dimensional (3D) simulations therefore allow for a direct comparison to experiments.

To test our approach we first compare results to the experiment [12], simulating the full experimental sequence illustrated in Fig. 1. We prepare finite temperature ini-

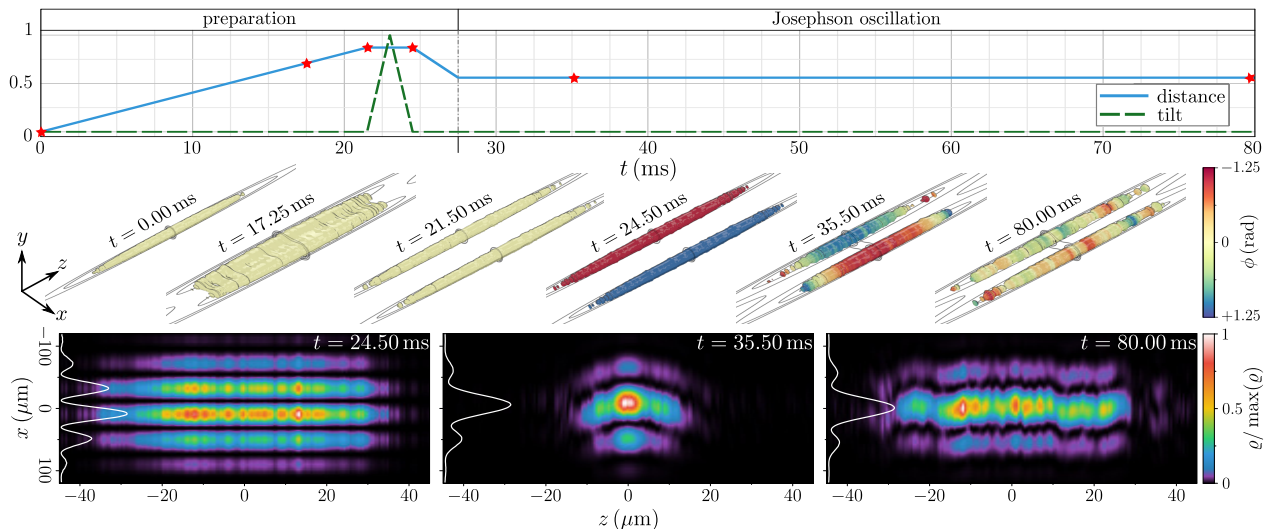


FIG. 1. Schematic of the experimental sequence [12]. Upper panel: During preparation a single condensate is coherently split (blue line shows the distance of the two wells). Once completely decoupled a tilt (dashed green line) in the y -direction introduces an energy difference between the wells resulting in the accumulation of a global phase difference Φ_0 . Thereafter, a variable coupling is achieved by reducing the distance on a short timescale, leading to the observed Josephson oscillations. Middle panel: Snapshots of the wavefunction at different times (red stars from left to right) for $N = 3500$ particles, $\Phi_0 = -1.25$ rad, and temperature $T \approx 20$ nK. The 3D figures show isosurfaces of the density (0.35 of the maximum value) with the local phase difference $\phi(\mathbf{r}, t)$ encoded in color. Grey lines show isolines of the external potential $U(\mathbf{r}, t)$. Lower panel: Interference pictures after finite time of flight with the normalized density depicted in color and the integrated (along the z -direction) contrast depicted in white. The almost straight interference fringes at $t = 80$ ms show relaxation to a phase locked state.

tial conditions for $\Psi(\mathbf{r}, 0)$ through the stochastic GPE evolution [24, 25]. We further implemented a time of flight simulation to investigate the time evolution of the interference pattern measured in the experiment. Consistent with [12] we obtain almost straight fringes after a few cycles of the oscillation, signaling the relaxation of the system to a phase locked state. We find excellent agreement between the global phase $\Phi(t)$ extracted from the interference pictures and calculated from the in situ phase differences [24]. Therefore, we consider in the following the in situ observables, omitting the time of flight expansion.

The time evolution of the local phase difference $\langle \phi(z, t) \rangle$ and the global phase $\langle \Phi(t) \rangle$ for typical experimental parameters is given in Fig. 2(a). The canonical conjugate atom number difference will be omitted for brevity. Here, $\langle \dots \rangle$ is the ensemble average over typically 300 independent realizations, where we additionally take into account fluctuations of the total atom number N in accordance with the experiment [24].

The spatial dependence of the Josephson frequency $\omega_J \equiv \omega_J[\rho(z)]$, decreasing towards the edges of the condensate, is clearly visible through the bending of the local phase difference. Therefore, different parts of the condensate exhibit local dephasing. This leads to a damping of the global phase difference $\Phi(t)$, even in the absence of dynamics along the longitudinal direction. Furthermore, atom number fluctuations contribute to an additional dephasing between different realizations due to the depen-

dence of the Josephson frequency ω_J on the total particle number N (see following section and [24]).

However, despite being a good approximation for the evolution of $\langle \Phi(t) \rangle$, these effects alone do not correctly describe the observed relaxation of the system.

Large atom number fluctuations lead to an increasing width in the full distribution function for the global phase $\Phi(t)$. At long times this causes significant damping for ensemble averaged observables. However, as can be seen in the polar histograms shown in Fig. 2(b), this spread remains small over the considered time period.

Moreover, local dephasing does not explain the observed local damping of $\phi(z, t)$. This can be clearly seen in the time evolution of the contrast $\mathcal{C}(t)$ (see Fig. 2(b)), here calculated from the in situ phase profiles [24, 26]. We find $\mathcal{C}(t)$ to increase at late times back close to its initial value which, consistent with [12], signals the relaxation to a phase locked state. Contrary, considering only local and atom number dephasing \mathcal{C} remains small despite the strongly damped global phase oscillations.

In order to compare our results to the experiment for varying initial conditions and tunneling strengths, we determine the damping time τ by fitting our numerical results with the model for a damped Josephson junction presented in [12]. In all cases we find our results to be compatible with the experiment (see Fig. 2(c)). This includes a relatively weak dependence of τ on the initial global relative phase Φ_0 , a plateau-shaped dependence on the effective tunnel coupling strength J , and approxi-

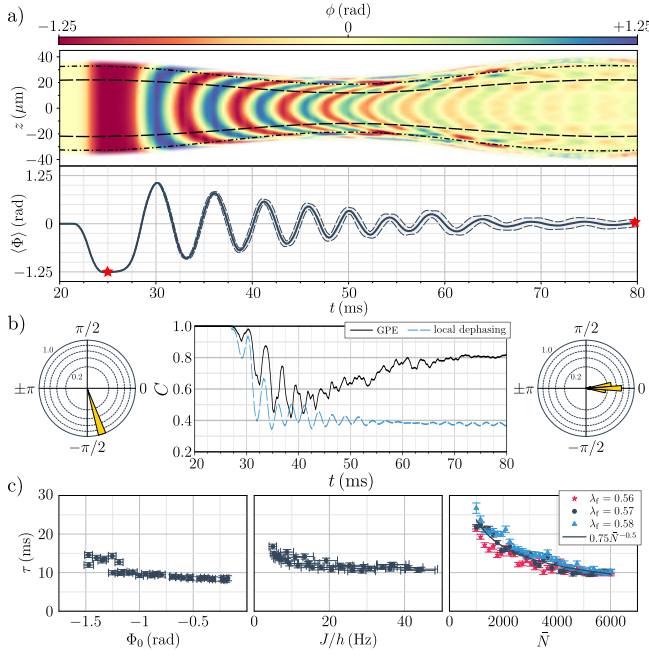


FIG. 2. Results of 3D-GPE simulations for $N = 3500(280)$, $T = 20$ nK, and $\Phi_0 = -1.25$ rad. (a) Upper panel: Ensemble average of the local phase difference $\langle \phi(z, t) \rangle$ (depicted in color) as a function of time and longitudinal coordinate z . Dashed (-dotted) lines mark the region containing 75% (95%) of atoms. Lower panel: Ensemble average of the global relative phase $\langle \Phi(t) \rangle$. Dashed lines depict the standard deviation. (b) Polar histograms of $\Phi(t)$ for the initial and final state (red stars in (a)) and contrast $\mathcal{C}(t)$ for the GPE simulation (black line) reveal relaxation beyond local and atom number dephasing (blue dashed line). See main text for details. (c) Dependence of damping time τ on the initial phase difference Φ_0 , tunneling strength J , and mean atom number \bar{N} are consistent with the experiment [12]. Errorbars depict the standard deviation and the final dressing amplitude λ_f determines the tunneling coupling (decreasing for larger λ_f).

mately $\tau \sim N^{-0.5}$. Note, however, that for the latter we find a slight additional dependence of the exponent on the single-particle tunneling coupling J .

Multimode dephasing & non-linear relaxation.—In order to study the fundamental mechanisms leading to the rapid local damping of Josephson oscillations, we consider in the following a zero-temperature ($T = 0$) state with fixed particle number $N = 3500$. We further omit the preparation phase to mitigate the effect of a common breathing excitation and imprint the phase difference directly in the final trap configuration.

These simplifications preserve the observed main results of rapid global and local damping of Josephson oscillations and enable us to compare results of the full 3D simulations with a tractable linearized, one-dimensional model (see e.g. [24, 27]). For a harmonically confined system in the Thomas-Fermi approximation, i.e. $\rho_0(z) = \rho_0[1 - (z/R)^2]$ with Thomas-Fermi radius R , we find an exact solution in terms of the angular oblate spheroidal

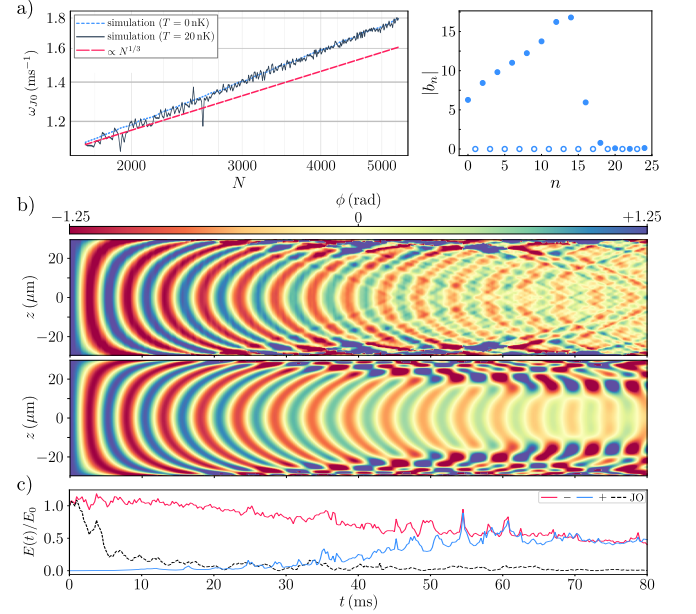


FIG. 3. Comparison and breakdown of the linearized 1D model. (a) Left panel: Dependence of the Josephson frequency ω_{J0} on the atom number N . The increased exponent ($\kappa > 1/3$) signals the nonlinear dependence on the mean field density. Right panel: Mode occupation $|b_n|$ for the first 25 modes in the 1D model. (b) Comparison of the phase difference $\phi(z, t)$ for the full 3D-GPE simulations (upper panel) and the 1D model (lower panel). System parameters are $N = 3500$, $T = 0$ nK, $\Phi_0 = -1.25$ rad, and $\omega_{J0} \approx 235$ s⁻¹. (c) Normalized energy in the symmetric (blue) and antisymmetric (red) degrees of freedom and the $k = 0$ mode (black dashed) reveal multimode dynamics and relaxation beyond the SG model (see main text for details). Note that, while the GPE obeys energy conservation, the depicted energies are calculated using Eq. (2) and hence are not strictly conserved.

wave functions [24, 28]. The mode frequencies ω_n are given in [24], featuring an increasing energy gap and twofold degeneracy of the spectrum for larger tunneling coupling J (cf. [27]).

Here, we neglected the non-linear density dependence of ω_J , i.e. assuming $\omega_J(z) = \sqrt{1 - (z/R)^2} \omega_{J0}$, for which the model only depends on the dimensionless Josephson frequency $\omega_{J0}/\omega_{||}$. We find the dominant effect of the non-linear density dependence to be a constant shift of ω_{J0} with the total atom number N . The most simple model for the case of a harmonic longitudinal confinement yields $\omega_{J0} \propto N^\kappa$ with $\kappa = 1/3$. However, by fitting a whole series of 3D simulations covering a wide range of atom numbers, we find $\kappa \approx 0.43$ (see Fig. 3(a)), indicating an interwell tunneling that depends on the local density of the quasicondensates. Note that this also increases the influence of trivial dephasing caused by atom number fluctuations. In the following we will treat ω_{J0} as a free parameter of our analytic model when comparing to GPE simulations.

The evolution of the local phase $\phi(z, t)$ for the full GPE

simulation and the analytic model are shown in Fig. 3(b). For the latter the time evolution is given by multimode dephasing of the initially populated free quasiparticle modes (see right panel in Fig. 3(a)). This multimode character leads to a rapid initial damping of the global Josephson oscillation, similar to the previous local dephasing. Most notably, however, the dephasing of free quasiparticle modes already leads to a local damping of oscillations. At early times, we find excellent agreement between the full numerical simulation and the analytic predictions. For later times the linearized theory shows oscillations increasing again in amplitude, which propagate inwards from the boundaries. These are caused by (partial) rephasing dynamics as a result of the limited number of quasiparticle modes with significant population [29].

The absence of rephasing in the full 3D simulations signals the breakdown of the linearized model, either through nonlinear terms in the SG model or coupling of the symmetric and antisymmetric degrees of freedom (DoF). For the former the Hamiltonian of the system is still given by

$$H \approx H_{\text{LL}}[\delta\rho_s, \phi_s] + H_{\text{SG}}[\delta\rho_a, \phi_a], \quad (2)$$

Here $\delta\rho_{s(a)}$ and $\phi_{s(a)}$ are the symmetric (antisymmetric) density and phase fluctuations, approximately described by the Luttinger Liquid (H_{LL}) and sine-Gordon (H_{SG}) Hamiltonian, respectively [9, 24]. Higher-order corrections couple the symmetric and anti-symmetric DoF leading to a transfer of energy between the two sectors. This signals a definite breakdown for the effective description of the extended Josephson junction through the SG model (Eq. (2)).

We quantify the coupling in Fig. 3(c), showing the time evolution of the energies within each sector. In addition, we display the energy of the zero-momentum ($k = 0$) mode of the antisymmetric DoF determining the spatially independent, global Josephson oscillation. Therefore, the initial energy E_0 is completely given by this zero-momentum mode.

At early times the energies are approximately conserved, validating a description in terms of Eq. (2). Consequently, the linearized model constitutes a good approximation in this regime, in accordance with Fig. 3(b). The rapid decline of the $k = 0$ mode is caused by the multimode dephasing, transferring energy to higher momentum states within the antisymmetric sector. Note that quasiparticle dephasing here leads to transport in momentum space since plane waves are not the eigenstates of the system.

For $30 \text{ ms} \lesssim t \lesssim 60 \text{ ms}$ energy transfer from the antisymmetric to the symmetric DoF becomes dominant, revealing the breakdown of the SG model. At later times the system reaches equipartition of energy. This does however not imply complete thermalization of the system. We like to highlight that significant coupling al-

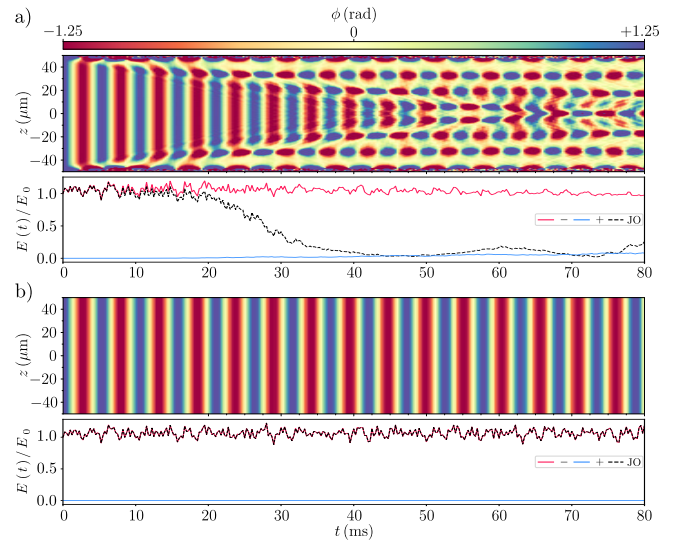


FIG. 4. Relaxation in flat-bottom potentials. Results for 3D-GPE simulations as in Fig. 3 for a box-shaped potential (a) and a ring-shaped potential (b) in the longitudinal z -direction. We adjusted the particle number N requiring equal Josephson frequencies $\omega_J(z=0)$ for all trapping potentials. In neither case the system relaxes to a phase locked state since coupling of symmetric and anti-symmetric degrees of freedom is highly suppressed. For (b) the Josephson oscillation completely decouples.

ready occurs at zero temperature due to the spatially inhomogeneous Josephson frequency. This is the dominant effect leading to the relaxation of the system to a phase locked state as observed in [12].

Flat-bottom potentials.—The rapid equipartition of energy, invalidating a description of the system in the form of Eq. (2), greatly impedes an analogue implementation of the SG model and its long time evolution. Based on the recent progress in shaping arbitrary trapping potentials in cold-atom experiments [30, 31] we now give an outlook on the possibilities for studying the (quantum) SG model in these systems.

We show in Fig. 4(a) the time evolution of $\phi(z, t)$ and the normalized energies for a box-shaped potential. Spatial dependence of the Josephson frequency is limited to the edges of the condensate leading to disturbances emanating from the boundaries. Once propagated inwards these disturbances lead to a rapid decline of the $k = 0$ mode caused by multimode dephasing. In contrast to the harmonic confinement, however, global Josephson oscillations prevail within the central region of the box (for $t \lesssim 20 \text{ ms}$). In particular, the amplitude of local phase oscillations remains high. Therefore, the contrast \mathcal{C} after its initial decrease remains small at longer times, i.e. the system does not relax to a phase locked state. Consistently, coupling between the symmetric and antisymmetric DoF is highly suppressed, with only $\approx 16\%$ of the energy being transferred at $t = 80 \text{ ms}$. Therefore, while the antisym-

metric DoF shows multimode dynamics a description in terms of Eq. (2) constitutes a good approximation.

Ring-shaped potentials further eliminate the influence of the boundaries, leading to undamped global Josephson oscillations at zero temperature (see Fig. 4(b)). In accordance, we find the total energy to remain in the $k = 0$ mode, with negligible coupling between the symmetric and antisymmetric DoF. Here, dephasing due to atom number fluctuations will dominate ensemble averages at late times, which can be mitigated through appropriate postselection. Naturally, this is the ideal setting to study the dynamics of the SG model including thermal and/or quantum fluctuations.

Conclusion.—In this Letter we gave a detailed discussion of the rich nonlinear dynamics in inhomogeneous extended bosonic Josephson junctions. Results of the full 3D-GPE simulations were found to be compatible with the experimental findings [12] over a wide range of parameters. We explained the relaxation to a phase locked state, as observed in [12], through the breakdown of the SG model description for harmonic confinements. Our results highlight the importance of understanding the classical nonlinear dynamics, even at zero temperature, before comparing results to sophisticated quantum models. Furthermore, we outline the experimental possibilities and steps necessary to study relaxation in extended bosonic Josephson junctions and the (quantum) sine-Gordon model out of equilibrium.

We acknowledge support by the Wiener Wissenschafts- und TechnologieFonds (WWTF), project No. MA16-066 (“SEQUEX”) and the Austrian Science Fund (FWF) via Grant SFB F65 (Complexity in PDE systems) and SFB 1225 Project-ID 273811115 (ISOQUANT). S.E. acknowledges support from the European Union’s Horizon 2020 research and innovation programme under the Marie Skłodowska-Curie grant agreement No 801110 and the Austrian Federal Ministry of Education, Science and Research (BMBWF) from an ESQ fellowship. This manuscript reflects only the authors’ view, the EU Agency is not responsible for any use that may be made of the information contained herein.

* erne@atomchip.org

- [1] S. Coleman, Phys. Rev. D **11**, 2088 (1975).
- [2] A. B. Zamolodchikov and A. B. Zamolodchikov, Annals of Physics **120** (1979).
- [3] J. Cuevas-Maraver, P. G. Kevrekidis, and F. Williams, Nonlinear Systems and Complexity (Switzerland: Springer) (2014).
- [4] A. M. Polyakov, Nuclear Physics B **120**, 429 (1977).
- [5] S. Samuel, Physical Review D **18**, 1916 (1978).
- [6] J. V. José, L. P. Kadanoff, S. Kirkpatrick, and D. R. Nelson, Physical Review B **16**, 1217 (1977).
- [7] F. H. Essler and R. M. Konik, in *From Fields to Strings: Circumnavigating Theoretical Physics: Ian Kogan Memorial Collection (In 3 Volumes)* (World Scientific, 2005) pp. 684–830.
- [8] J. Berges, S. Floerchinger, and R. Venugopalan, Journal of High Energy Physics **2018**, 145 (2018).
- [9] V. Gritsev, A. Polkovnikov, and E. Demler, Physical Review B **75**, 174511 (2007).
- [10] T. Schweigler, V. Kasper, S. Erne, I. Mazets, B. Rauer, F. Cataldini, T. Langen, T. Gasenzer, J. Berges, and J. Schmiedmayer, Nature **545**, 323 (2017).
- [11] T. V. Zache, T. Schweigler, S. Erne, J. Schmiedmayer, and J. Berges, Physical Review X **10**, 011020 (2020).
- [12] M. Pigneur, T. Berrada, M. Bonneau, T. Schumm, E. Demler, and J. Schmiedmayer, Physical review letters **120**, 173601 (2018).
- [13] S. Levy, E. Lahoud, I. Shomroni, and J. Steinhauer, Nature **449**, 579 (2007).
- [14] R. Gati and M. Oberthaler, Journal of Physics B: Atomic, Molecular and Optical Physics **40**, R61 (2007).
- [15] L. LeBlanc, A. Bardon, J. McKeever, M. Extavour, D. Jervis, J. Thywissen, F. Piazza, and A. Smerzi, Physical review letters **106**, 025302 (2011).
- [16] N. K. Whitlock and I. Bouchoule, Physical Review A **68**, 053609 (2003).
- [17] Y. D. van Nieuwkerk and F. H. Essler, arXiv preprint arXiv:2003.07873 (2020).
- [18] Y. D. van Nieuwkerk, J. Schmiedmayer, and F. H. Essler, arXiv preprint arXiv:2010.11214 (2020).
- [19] E. G. Dalla Torre, E. Demler, and A. Polkovnikov, Physical review letters **110**, 090404 (2013).
- [20] L. Foini and T. Giamarchi, The European Physical Journal Special Topics **226**, 2763 (2017).
- [21] Y. D. van Nieuwkerk and F. H. Essler, Journal of Statistical Mechanics: Theory and Experiment **2019**, 084012 (2019).
- [22] D. Horváth, I. Lovas, M. Kormos, G. Takács, and G. Zaránd, Physical Review A **100**, 013613 (2019).
- [23] L. Pitaevskii and S. Stringari, *Bose-Einstein condensation and superfluidity*, Vol. 164 (Oxford University Press, 2016).
- [24] See Supplemental Material for details.
- [25] P. B. Blakie, A. Bradley, M. Davis, R. Ballagh, and C. Gardiner, Advances in Physics **57**, 363 (2008).
- [26] V. Gritsev, E. Altman, E. Demler, and A. Polkovnikov, Nature Physics **2**, 705 (2006).
- [27] M. Momme, Y. Bidasyuk, and M. Weyrauch, Physical Review A **100**, 033601 (2019).
- [28] A. M and I. A. Stegun, *Handbook of Mathematical Functions* (National Bureau of Standards, Washington, DC, 1964) Chap. 12, 21.
- [29] B. Rauer, S. Erne, T. Schweigler, F. Cataldini, M. Tajik, and J. Schmiedmayer, Science **360**, 307 (2018).
- [30] M. Tajik, B. Rauer, T. Schweigler, F. Cataldini, J. Sabino, F. S. Møller, S.-C. Ji, I. E. Mazets, and J. Schmiedmayer, Optics Express **27**, 33474 (2019).
- [31] W. Heathcote, E. Nugent, B. Sheard, and C. Foot, New Journal of Physics **10**, 043012 (2008).

SUPPLEMENTAL MATERIAL

Simulation of the original experiment

Our numerical simulation follows closely the experiment in [12] where the extended bosonic Josephson junction was realized through an ultracold gas of ^{87}Rb atoms in an adjustable double-well potential on an atom chip. The gas was cooled well below degeneracy, such that the evolution of the system can be described by means of the Gross–Pitaevskii equation (Eq. (1)) with finite temperature initial conditions. Details of the theoretical description and numerical implementation are discussed in the following sections. Here we give an overview of the numerical procedure and our data analysis simulating the original experiment.

As a model for the trapping potential $V(\mathbf{r}, t)$ we use the adiabatic radio-frequency potential on an atom chip [32]. The double-well is controlled by two external time-dependent parameters $u_1(t)$ and $u_2(t)$. These adjust the distance (in x -direction) and tilt (in y -direction) between the two wells, respectively. The final dressing amplitude u_1 for $t \geq 27.5$ ms determines the Josephson frequency ω_{J0} and is denoted by λ_f in Fig. 2(c) of the main text. Along the longitudinal axis (z -direction) the original experiment [12] has a harmonic confinement with frequencies $\nu_{\parallel} = 22$ Hz and $\nu_{\parallel} = 12$ Hz for the initial (single-well) and final (double-well) potentials. The radial trapping frequencies are $\nu_{\perp} \approx 3$ kHz and $\nu_{\perp} \approx 1.5$ kHz for the initial and final traps, respectively, such that the system is close to the 1D regime $\mu, k_B T \ll \hbar\omega_{\perp}$.

The experimental sequence is depicted in Fig. 5(a). The trap begins to split at $t > 0$ and approaches at $t = 21.5$ ms its double-well configuration corresponding to the largest distance of the two halves of the quasicondensate. Next, a tilt along the transverse direction of the trap induces a global phase difference between the two separated atom clouds. Finally, within the period of $t = 24.5$ ms and $t = 27.5$ ms the distance of the two halves of the condensate is lowered and the system starts to oscillate.

The numerical stability is demonstrated in Fig. 5(b) for a selected single run (with $N = 3500$ and $T = 20$ nK). The total energy E is conserved as long as the control inputs u_1 and u_2 remain unchanged (i.e. the Hamiltonian is time-independent). Also the number of atoms N is nicely conserved throughout the whole simulation as it is expected for the time-splitting algorithm used here to solve the GPE. Furthermore, the figure shows the effective length ℓ of the condensate encompassing 95% of total particles N . The period of the observed breathing mode agrees reasonably well with the theoretical prediction for a one-dimensional condensate $T_b \approx 48$ ms using $\nu_b = \sqrt{3}\nu_z$ with $\nu_z = 12$ Hz.

Expectation values of observables are calculated from

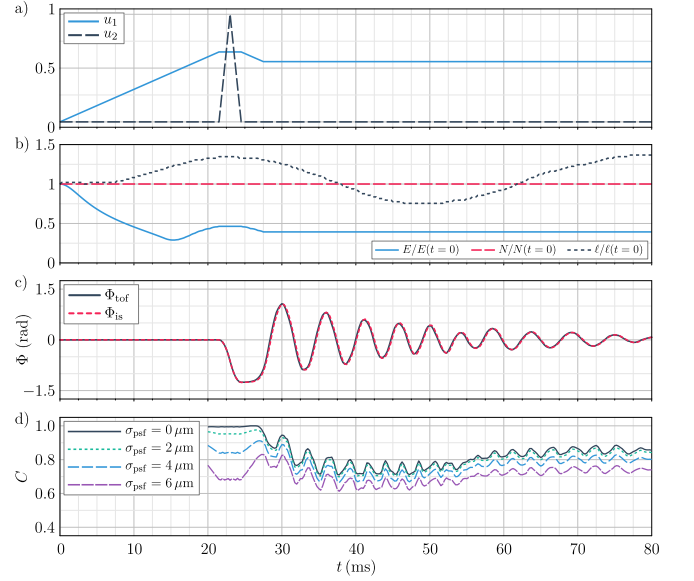


FIG. 5. Numerical results corresponding to a selected single run of a simulation using the original experimental procedure described in [12]. a) Distance and tilt between the two wells controlled by u_1 (solid blue) and u_2 (dashed black), respectively. The final value of u_1 determines the distance and hence the tunneling strength ω_{J0} between the two halves of the condensate. b) Total energy E , atom number N , and effective length ℓ of the condensate. c) Global relative phase Φ_{tof} as a result of TOF-simulations and global relative phase Φ_{is} using the (in situ) wave function. d) Contrast C extracted from the integrated profiles in TOF-simulations for different experimental resolutions σ_{PSF} .

the ensemble averages over typically $n_{\text{sr}} = 301$ independent realizations used to sample the (restricted) atom number distribution and the thermal noise in the initial conditions. Note that due to the large number of different parameters we use $n_{\text{sr}} = 21$ in Fig. 2(c) of the main text. Convergence of the extracted values were checked for selected random parameters for larger values of n_{sr} .

Interference pictures and global phase extraction

In the experiment, the evolution of the system is investigated by destructive measurements after time-of-flight (TOF) either looking at the interference pictures or the atom number difference between the two wells. We calculate the TOF expansion numerically, taking atom interactions into account for the first millisecond of the expansion. During this time, the system rapidly expands along the tightly confined radial direction, diluting the gas sufficiently such that the expansion becomes ballistic (i.e. non-interacting). Once the TOF-expansion has been computed, we integrate the density along the vertical direction y to obtain the desired interference pictures measured in the experiment. Additionally, to account

for the finite imaging resolution in the experiment, we include a convolution of the numerical interference pictures with a Gaussian point-spread function

$$\xi(x, z) = \exp(-(x^2 + z^2)/(2\sigma_{\text{psf}}^2))/(2\pi\sigma_{\text{psf}}^2)$$

The local relative phase $\phi(z, t)$ can be extracted by fitting a sinusoidal function to each pixel along the longitudinal z -direction. Finally, integrating along the longitudinal z -direction to obtain the profile $n_p(x)$, the contrast C and the global relative phase Φ_{tof} are determined using

$$n_p(x) \approx A \exp(-x^2/(2\sigma^2))(1 + C \cos(kx - \Phi_{\text{tof}})), \quad (3)$$

where A , σ , C , k and Φ_{tof} are found by solving a nonlinear least squares problem.

The time evolution of the global phase Φ_{tof} is shown in Fig. 5(c). Furthermore, the effect of the point spread function on the contrast C is depicted in Fig 5(d) for various values of σ_{psf} . The behavior is consistent with the results presented in Fig. 2(b) of the main text and similar to the original experiment, showing a fast initial decrease of the contrast followed by a restoration almost back to its initial value signaling the relaxation to a phase locked state.

In situ observables

The computation of the global relative phase Φ_{tof} by means of a TOF-simulation and formula (3) is a time-consuming process. Alternatively, the global relative phase can be extracted from the in situ wave function directly via

$$\Phi_{\text{is}} = \arg \left[\int_0^\infty dx \int_{-\infty}^\infty dy \int_{-\infty}^\infty dz \Psi(x, y, z) \Psi^*(-x, y, z) \right]. \quad (4)$$

In Fig. 5 (c) we compare the global relative phase Φ_{is} using the in situ wave function and definition (4) to Φ_{tof} extracted from the interference pictures after finite TOF. The results of both methods are practically indistinguishable and the weighting implicitly applied in formula (4) reflects the weighting involved in the procedure using the TOF-images reasonably well. We therefore omitted the TOF expansion for the results presented in the main text.

The local phase profiles $\phi(z, t)$ can be defined omitting the integration over z in Eq. (4). Due to coherence along the tightly confined radial direction, the results are reasonably close to the line values

$$\phi(z) = \arg [\Psi(x_1, 0, z) \Psi^*(x_2, 0, z)] , \quad (5)$$

used in the main text. Here x_1 and x_2 are at the minimum of the radial potential in the left and right well (i.e. at the points of maximum density), respectively. The

contrast C reported in the main text is computed from the in situ phase differences via

$$C(t) = \text{Re} \left[\int dz \int dz' \langle e^{-i(\phi(z) - \phi(z'))} \rangle \right], \quad (6)$$

where we neglected the strongly suppressed density fluctuations [26].

Simulations omitting the preparation phase

The coherent splitting of a single condensate leads to the excitation of a common breathing mode, due to the halving of the atom number within each well. In order to reduce its influence on the relaxation dynamics and enable us to compare numerical results to an analytically tractable model we omitted in Figs. 3 & 4 the preparation phase ($t < 27.5$ ms). Here we initialize the system directly in the final trap configuration ($t = 27.5$ ms) and imprint the initial phase difference manually. For the flat-bottom potentials considered in Fig. 4 of the main text we use a box shaped potential with finite wall width and a periodic ring potential instead of the harmonic longitudinal confinement, respectively. As for the harmonic confinement, the double-well distance and tilt are controlled by $u_1(t)$ and $u_2(t)$, respectively. The data analysis during the oscillation phase proceeds as described above.

Theoretical models

Effective 1D equations

The full 3D dynamics of the system is described by the GPE, given in Eq. (1) of the main text. In order to arrive at an analytically tractable model we first proceed with the common dimensional reduction, reducing the system to two one-dimensional coupled quantum wires by integrating over the transverse directions [33, 34]. Regaining the dominant terms in the expansion, the system of two coupled 1D GPE equations can be described by the Hamiltonian

$$H_{1D} = \int dz \sum_{i=1,2} \left[\psi_i^\dagger(z) H_{\text{GP}} [\psi_i] \psi_i(z) \right] - \psi_1^\dagger \mathcal{J} [\psi_1, \psi_2] \psi_2 + \text{H.c.} . \quad (7)$$

Here $\psi_{1(2)}$ is the field in the left (right) well of the double-well potential described by

$$H_{\text{GP}} [\psi_i] = -\frac{\hbar^2}{2m} \partial_z^2 + V(z) + \frac{g_{1D}}{2} |\psi_i(z)|^2 , \quad (8)$$

where $g_{1D} \approx 2\hbar a_s \omega_\perp$ is the effective 1D interaction constant and

$$\mathcal{J} [\psi_1, \psi_2] = \hbar J + \frac{\hbar F}{2} [|\psi_1|^2 + |\psi_2|^2] \quad (9)$$

is the tunneling coupling, including the dominant non-linear density dependence (see e.g. [27] for details). In general we have $|J| \gg |F \max[\rho_0]|$. Note, in particular, that also J can show an explicit density dependence due to radial swelling of the condensate [34].

Next, writing the fields in the Madelung representation $\psi_i = \sqrt{\rho_0 + \delta\rho_i} e^{i\phi_i}$, we expand the Hamiltonian in the small density perturbations $\delta\rho$ and phase gradients $|\partial_z\phi|$ (where $|\dots|$ denotes the typical value) [35]. To second order this allows us to separate the symmetric and anti-symmetric degrees of freedom. Further, upon neglecting the quantum pressure term, this leads to

$$H_{1D}^{(2)} \approx H_{LL}[\delta\rho_s, \phi_s] + H_{sG}[\delta\rho_a, \phi_a] , \quad (10)$$

where

$$\phi_s = \frac{1}{2}(\phi_1 + \phi_2) \quad \phi_a = \phi_1 - \phi_2 \quad (11)$$

$$\delta\rho_s = \delta\rho_1 + \delta\rho_2 \quad \delta\rho_a = \frac{1}{2}(\delta\rho_1 - \delta\rho_2) , \quad (12)$$

and H_{LL} and H_{sG} are the Luttinger-Liquid and sine-Gordon Hamiltonians, respectively. In the previous section and the main text we dropped the subscript ‘ a ’ when there is no risk of confusion.

The energies of the (anti-)symmetric DoFs ($i = s, a$) depicted in Fig. 3(c) and Fig. 4 of the main text are given by

$$E_i = \int dz \left[-\frac{\hbar^2}{4m} \left[\zeta_i^2 (\partial_z \delta\rho_i)^2 + \frac{\rho_0^2}{\zeta_i^2} (\partial_z \phi_i)^2 \right] + \zeta_i^2 g_{1D} \delta\rho_i^2 - \delta_{ia} \left[\hbar J \rho_0 (\cos(\phi_a) - 1) + \frac{\hbar J \delta\rho_a^2}{2\rho_0} \cos(\phi_a) \right] \right] , \quad (13)$$

where we suppressed the spatial and temporal dependence of the fields $\delta\rho(z, t)$, $\phi(z, t)$, and $\rho_0(z)$ for simplicity. Here $\zeta_{s(a)} = 0.5(1)$ for the symmetric and anti-symmetric DoF, δ_{ia} is the Kronecker delta, and we included the quantum pressure and minor coupling correction (first and last term respectively) for completeness.

Solutions to the linearized EoM

We present an analytic solution to the linearized equations of motion for a harmonically trapped system. Under the assumption of (i) the Thomas-Fermi approximation $\partial_z \rho_0 / \rho_0 \ll 1$, (ii) neglecting nonlinear density dependence of the tunneling coupling, and (iii) small tunneling energy compared to the chemical potential $\hbar J / \mu \ll 1$ the linearized equations of motion for the relative phase field obey the eigenvalue equation

$$\partial_x [(1 - x^2) \partial_x \phi] + [\lambda_{0n}^2 - \gamma^2 (1 - x^2)] \phi = 0 , \quad (14)$$

where we assumed $\phi(t) \sim e^{i\omega_n t}$ and defined the eigenvalue $\lambda_{0n} = \sqrt{2}\omega_n / \omega_{||}$, the dimensionless Josephson frequency $\gamma = \sqrt{2}\omega_{J0} / \omega_{||}$, and the dimensionless spatial coordinate $x = z/R$, where R is the Thomas-Fermi radius.

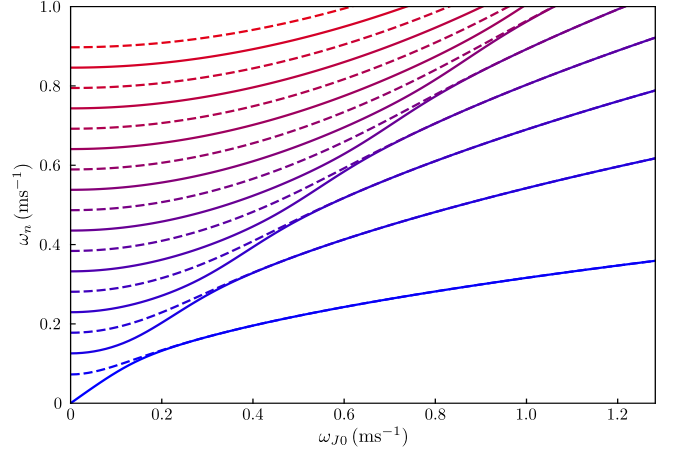


FIG. 6. Frequencies ω_n for the first 16 eigenmodes of the linearized model Eq. (14) as a function of the tunneling coupling ω_{J0} . Even (odd) modes are depicted with solid (dashed) lines.

Exact solutions to Eq. (14) are given by the angular oblate spheroidal wave functions S_{mn} for $m = 0$ [28]. The eigenfrequencies ω_n are depicted in Fig. 6. For $\gamma = 0$ Eq. (14) reduces to the Legendre differential equation [36]. Imposing canonical commutation relations for $\delta\rho_a$ and ϕ_a determines the normalization of the mode functions and leads to the mode expansion of the phase and density quadratures

$$\phi = \sum_n \sqrt{\frac{(2n+1)\mu}{2R_{TF}\hbar\omega_n\rho_0}} S_{0n}(x) b_n e^{i\omega_n t} + \text{H.c.} \quad (15)$$

$$\delta\rho = \sum_n \sqrt{\frac{(2n+1)\hbar\omega_n\rho_0}{2R_{TF}\mu}} S_{0n}(x) b_n e^{i\omega_n t} + \text{H.c.} \quad (16)$$

We calculate the occupation number $|b_n|$ presented in Fig. 3(a) of the main text by projecting the initial constant phase difference Φ_0 onto the quasiparticle basis Eq. (15).

For the evolution of the global phase $\Phi(t)$ an approximate analytic expression can be found by neglecting the first term in Eq. (14) (i.e. assuming the kinetic energy to be a small perturbation). The solution $\phi(z, t) = \phi_0 \cos(\sqrt{1 - x^2}\omega_J t)$ describes an assembly of independent Josephson junctions with local frequencies. The global relative phase in the absence of breathing motion can be expressed as

$$\begin{aligned} \Phi(t) &= \frac{1}{2} \int_{-1}^1 dx \phi_0 \cos\left(\sqrt{1 - x^2}\omega_J t\right) \\ &= \phi_0 \frac{\pi}{2} \mathbf{H}_{-1}(\omega_J t) , \end{aligned} \quad (17)$$

where $\mathbf{H}_\alpha(\tau)$ is the Struve function of the order α [28].

Eq. (17) can be extended to include fluctuations of the Josephson frequency, e.g. caused by atom number

fluctuations. Assuming a uniform distribution in ω_J on the interval $[\bar{\omega}_J(1 - \eta), \bar{\omega}_J(1 + \eta)]$ with $\eta \ll 1$ this leads to

$$\begin{aligned} \langle \Phi(t) \rangle_N^{\text{theor}} &= \frac{1}{2\eta\bar{\omega}_J} \int_{\bar{\omega}_J(1-\eta)}^{\bar{\omega}_J(1+\eta)} d\omega_J \phi_0 \frac{\pi}{2} \mathbf{H}_{-1}(\omega_J t) \\ &= \phi_0 \frac{\pi}{2} \frac{\mathbf{H}_0[\bar{\omega}_J t(1 + \eta)] - \mathbf{H}_0[\bar{\omega}_J t(1 - \eta)]}{2\eta\bar{\omega}_J t}. \end{aligned} \quad (18)$$

It is worth pointing out that fitting Eq. (18) to the ensemble average $\langle \Phi(t) \rangle$ of our full numerical simulations, we find η to be reasonably close (within $\approx 10\%$) to its expected value $\eta = \kappa \delta_N / \bar{N}$ with $\kappa \approx 0.43$.

Numerical Methods

Confinement potentials

Harmonic potential—We consider an adiabatic radio-frequency potential presented in [32] approximating the experimentally measured potential as reported in [12]. Note, that this potential is in general non-separable, leading to further approximations when reducing the effective dimension of the system. An explicit implementation of the potential is available from the first author upon reasonable request. The tilt in y -direction is implemented via

$$V(x, y, z, t) = V(x, y, z, t) - u_2(t)x.$$

Box potential—The box potential is modeled by a separable function of the form

$$V_b(x, y, z, t) = V_1(x, y, t)V_2(z)$$

where $V_1(x, y, t)$ denotes the time-dependent confinement potential of the harmonic trap

$$V_1(x, y, t) = V(x, y, z = 0, t)$$

at $z = 0$ and $V_2(z)$ is given by a smoothed box-like function

$$V_2(z) = \frac{A}{2} \left[\tanh(s(|z| - w/2)) + 1 \right]$$

with the parameters $A = 1 \times 10^{-29}$, $s = 0.5 \times 10^6$ and $w = 100 \times 10^{-6}$.

Ring-shaped potential—The confinement potential of the ring-like structure is modeled by the function

$$V_r(x, y, z, t) = V_1(x, y, t)$$

where $V_1(x, y, t)$ denotes the time-dependent potential of the harmonic trap at $z = 0$. We note that this model represents an idealized version of a sufficiently large ring system such that the effect of the local curvature on the condensate can be neglected.

Time-Evolution

The Gross-Pitaevskii equation (GPE) is solved numerically by means of a time-splitting spectral (split-step Fourier) method which is based on a second order accurate operator splitting (Strang splitting) [37, 38]. Provided that the potential $U(\mathbf{r}, t)$ and the initial condition $\Psi(\mathbf{r}, 0) = \Psi_0(\mathbf{r})$ are sufficiently smooth functions, the spatial approximation converges at an exponential rate with respect to the maximum of the spatial resolutions Δx , Δy and Δz .

The algorithm can be easily implemented on a graphics processing unit (GPU) resulting in a dramatic speed-up in comparison with a CPU-based implementation. This reduction in computing time is essential for a successful simulation of the original experiment as the three-dimensional problem is needed to be solved for many realizations. Each realization represents an independent single run using a different initial value.

Ground state

A ground state solution of the Gross-Pitaevskii equation is computed using imaginary time propagation [39], requiring that the time step size Δt in the time-splitting spectral method is replaced by $-i\Delta t$. Furthermore, the wave function is normalized to a desired atom number N after every time step. The atom number distribution is assumed to be a normal distribution $f(N) = \mathcal{N}(\bar{N}, \sigma_N^2)$ with the mean \bar{N} and standard deviation $\sigma_N = 0.16 \bar{N}$. In the original experiment postselection further restricts the atom numbers to the range $[\bar{N} - \delta_N, \bar{N} + \delta_N]$ with a given cut-off parameter $\delta_N = 0.08 \bar{N}$. In the numerical simulations the restricted atom number distribution is obtained by inversely sampling the cumulative distribution function $F(N)$ over the interval $[F(\bar{N} - \delta_N), F(\bar{N} + \delta_N)]$ using an equidistant distribution of n_{sr} points representing the total number of single runs.

Thermal State Sampling

For finite temperature initial states, the resulting zero temperature ground state solutions are additionally propagated using the stochastic Gross-Pitaevskii equation (SGPE) (see e.g. [25] and references therein)

$$\begin{aligned} i\hbar \frac{\partial}{\partial t} \Psi(\mathbf{r}, t) &= (1 - i\gamma) \left[-\frac{\hbar^2}{2m} \nabla^2 + U(\mathbf{r}, 0) \right. \\ &\quad \left. + g|\Psi(\mathbf{r}, t)|^2 - \mu \right] \Psi(\mathbf{r}, t) + \eta(\mathbf{r}, t) \end{aligned} \quad (19)$$

until a new quasi-stationary thermal state is reached. Here, μ denotes the chemical potential of the eigenvalue problem at zero temperature and η is a complex random noise term. For the simple growth SGPE considered here,

the positive constant γ can be freely tuned to improve the speed of convergence. We keep the atom number fixed within each SGPE realization by normalizing the wave function after each time step. This is done to preserve the exact atom number distribution already included in the above calculation of the ground state for each realization. Including the fluctuations of the SGPE would, however, only lead to a small broadening of the atom number distribution. The SGPE can be solved using the same numerical method which is used to solve the ordinary GPE if the thermal noise term η is assumed to be constant for the duration Δt of every time step. Depending on the desired temperature, several tens of thousands of time steps are necessary to reach a quasi-stationary thermal state.

In the simplest approximation, η denotes a complex, Gaussian, white noise process with correlations

$$\langle \eta^*(\mathbf{r}, t) \eta(\mathbf{r}', t') \rangle = 2\hbar\gamma k_B T \delta(\mathbf{r} - \mathbf{r}') \delta(t - t') \quad (20)$$

corresponding to a given temperature T . However, using the noise term in form of Eq. (20) results in unrealistic excitations of the quasicondensate along the tightly confined transverse directions of the trap. One obvious solution to this problem is to project the wave function onto a few of the lowest energy single particle eigenstates of the harmonic trap. However, this approach, which is known as the projected stochastic Gross-Pitaevskii equation [25], is prohibitively expensive in our three-dimensional setting. Due to the extremely strong transverse confinement of the initial trap $k_B T \ll \hbar\omega_\perp$, the main effect of radially excited single particle states is an increase in width of the Gaussian ground state wave function [34]. We therefore expect the desired thermal state to be an almost perfectly symmetric and smooth function with respect to the transverse directions x and y .

This assumption can be taken into account in the preparation of the thermal noise $\eta(\mathbf{r}, t)$ in Eq. (19). In this context, we first compute a complex field $\Psi^\perp(x, y, z) = \Psi(x, y, z)/\sqrt{\rho(z)}$ using the 1D density

$$\rho(z) = \int \int |\Psi(x, y, z)|^2 dx dy$$

along the z -direction. For the noise term we finally employ the expression

$$\eta(x, y, z) = \lambda(z) \Psi^\perp(x, y, z),$$

where $\lambda(z)$ is one-dimensional Gaussian white noise with zero mean and variance given by Eq. (20) replacing $\delta(\mathbf{r} - \mathbf{r}')$ with $\delta(z - z')$. Convergence to the correct thermal state was verified by further evolving the system with the GPE after slightly disturbing the exact symmetry of the prepared states in the x, y -plane.

Time of flight

The calculation of TOF-images is a two-stage process. In the first stage we solve the GPE (1) including the nonlinear interaction potential for a period of $\mathcal{T}_1 = 1$ ms with the confinement potential V being set to zero. Within this time span the BEC expands considerably along the transverse directions x and y . To take into account this expansion, the complex array representing the wave function Ψ is first copied into a much larger computational domain. As the spatial resolution needs to be kept constant, the number of grid points increases massively and thus the numerical costs of the subsequent numerical propagation are significant.

At the end of the first stage the density has decreased to such an extent that the nonlinear term in the GPE can be neglected. Consequently, only the linear free Schrödinger equation needs to be solved in the second stage. An approximate solution can be computed by taking advantage of the fact that the spatial distribution approaches the momentum distribution of the initial condensate wave function as time tends to infinity, see, e.g., [40]. If the period until a TOF-image is taken is rather short, it is highly recommended to solve the original free Schrödinger initial value problem. Here, we consider a free expansion period of another $\mathcal{T}_2 = 19$ ms. While in theory, this problem can be solved most easily by the application of two Fourier transforms and a simple pointwise multiplication, in practice one faces severe computer memory issues. For more details on these issues and how they can be overcome we would like to refer to [40].

Imprinting the initial phase difference manually

As mentioned in the previous sections, we found that the original experimental procedure causes the excitation of a breathing mode which comes along with a global variation of the density and thus a modulation of the frequency of the Josephson oscillation. As this problem is mainly caused by the preparation phase, we may also consider to skip the preparation phase and instead imprint the initial phase difference manually. To this end, the initial wave function is multiplied by the factor $\exp(-i\Delta\phi)$ before starting the simulation of the oscillation phase. The phase shift $\Delta\phi = \phi_0 \arctan(x/d_0)/\pi$ represents a smoothed step function of the transverse coordinate x with a properly chosen maximum value ϕ_0 and a smoothing parameter $d_0 = 1.2 \times 10^{-7}$. To imprint a desired global relative phase Φ_0 , the value of ϕ_0 is chosen slightly larger than the desired global relative phase Φ_0 to approximately compensate for the fact that $\Delta\phi \approx 0$ in a region near $x = 0$.

* erne@atomchip.org

- [32] I. Lekanovsky, T. Schumm, S. Hofferberth, L. M. Andersson, P. Krüger, and J. Schmiedmayer, *Physical Review A* **73**, 033619 (2006).
- [33] M. Olshanii, *Physical review letters* **81**, 938 (1998).
- [34] L. Salasnich, A. Parola, and L. Reatto, *Physical Review A* **65**, 043614 (2002).
- [35] C. Mora and Y. Castin, *Physical Review A* **67**, 053615 (2003).
- [36] D. Petrov, G. Shlyapnikov, and J. Walraven, *Physical Review Letters* **85**, 3745 (2000).
- [37] W. Bao, D. Jaksch, and P. A. Markowich, *Journal of Computational Physics* **187**, 318 (2003).
- [38] W. Bao, S. Jin, and P. A. Markowich, *SIAM Journal on Scientific Computing* **25**, 27 (2003).
- [39] M. L. Chiofalo, S. Succi, and M. Tosi, *Physical Review E* **62**, 7438 (2000).
- [40] P. Deuar, *Computer Physics Communications* **208**, 92 (2016).